ROYAL SOCIETY
OF CHEMISTRY

PAPER

Check for updates

Dynamics of inverse metal oxides on metal catalysts using spectro-kinetics: reversible Brønsted acid site formation and irreversible reduction

Sagar Sourav,[ab] Jiahua Zhou,[bc] Quentin Kim,[bc] Kewei Yu, [iD][bc] Weiqing Zheng [iD][d] and Dionisios G. Vlachos [iD]*[cd]

Brønsted acid sites (BASs) in inverse catalysts are vital for the selective hydrogenolysis of polyols, specifically cleaving secondary C–O bonds. These BASs form dynamically *in situ* in an H_2 environment. While H_2 enables rapid BAS generation on short timescales, it reduces the catalyst at prolonged exposures. The active center for BAS generation, the kinetics of BAS formation, its reverse decomposition, and the irreversible oxide reduction have lacked direct experimental evidence. Here, aided by advanced spectro-kinetic studies, we identify trimeric W_3O_x sites on Pt as the active centers for BAS generation, whereas isolated WO_x species on SiO_2 act merely as spectator species, demonstrated using an inverse WO_x/Pt catalyst as a representative system. A detailed kinetic profile capturing the dynamics of W_3O_x sites on Pt is also established. The rate constant for BAS formation is two orders of magnitude higher than for its decomposition, which is one order of magnitude faster than the irreversible site reduction. Co-fed H_2O suppresses the site reduction by ~50%. Furthermore, the H_2 partial pressure plays an important role. While lower gas-phase H_2 partial pressure does not influence the reversible BAS formation, it can significantly (~3×) suppress catalyst reduction. These findings offer critical insights into optimizing reaction conditions through periodic H_2 pulsing, enhancing catalyst stability and performance in hydrogenolysis reactions.

Introduction

Metal–metal oxide (M–MO) catalysts are pivotal in petrochemical, fine chemical, pharmaceutical, and biomass upgrading reactions.[1–8] They typically combine noble metals like Pt, Ir, and Rh with oxophilic metal oxides such as WO_x, ReO_x, and MoO_x on top.[9,10] Their multiple surface functionalities—including Brønsted acid (BAS), Lewis acid (LAS), redox, and metallic sites—enable selective catalysis through synergistic interactions.[3,11,12] Among these, supported WO_x/Pt inverse catalysts[13,14] have garnered attention for alkane skeletal isomerization,[15] NO_x reduction,[16] biomass-derived chemical production,[17] and plastic upcycling.[18]

Recent advances employing *in situ/operando* characterization, density functional theory (DFT) calculations,

and probe chemistries have shed light on the structure and functionality of supported WO_x/Pt catalysts.[9,10,13,14,19] For instance,[19] *in situ* diffuse reflectance infrared Fourier transform spectroscopy (DRIFTS) with CO as a probe molecule and high-resolution transmission electron microscopy (HR-TEM) revealed that in oxidizing environments, WO_x predominantly remains anchored on the SiO_2 support while Pt exists as oxidized PtO_x. Reduction with CO facilitates the near-complete reduction of PtO_x without significantly altering the WO_x anchoring. In contrast, H_2 reduces Pt sites completely and decorates them with WO_x due to strong metal-support interaction (SMSI). CO-DRIFTS and probe chemistry studies further suggested that well-coordinated Pt sites favor WO_x decoration, while under-coordinated sites are energetically unfavorable for anchoring WO_x.[19]

Additional insights from *in situ* Raman spectroscopy and DFT calculations[13] highlighted the conceivable formation of oligomeric, best represented as trimeric W_3O_x, species on Pt surfaces, a significant departure from the traditional structure of WO_x on SiO_2. On SiO_2 supports, tungsten oxide (WO_x) exists exclusively as isolated surface species up to the monolayer coverage, beyond which three-dimensional WO_3

[a] *Department of Chemical Engineering, Indian Institute of Technology Madras, Chennai, Tamil Nadu 600036, India*
[b] *Delaware Energy Institute, University of Delaware, Newark, Delaware 19716, USA*
[c] *Department of Chemical and Biomolecular Engineering, University of Delaware, Newark, Delaware 19716, USA. E-mail: vlachos@udel.edu*
[d] *Delaware Energy Institute, Center for Plastics Innovation, University of Delaware, Newark, Delaware 19716, USA*

nanoparticles form.[20] This has been conclusively demonstrated by Wachs and co-workers through *in situ* Raman, UV–vis, and XAS analyses showing the absence of W–O–W vibrations and second-shell W coordination below the monolayer coverage. In contrast, when WO_x is supported on Pt/SiO_2, the interaction between WO_x and Pt nanoparticles gives rise to distinct structural motifs. Our prior studies revealed that WO_x on Pt predominantly adopts a W_3O_9 cluster configuration rather than monomeric (W_1O_x) or dimeric (W_2O_6) species. This assignment is supported by CO chemisorption (indicating sub-monolayer WO_x coverage), Raman spectra (showing both W–O–W and tetrahedral W=O vibrations around 800 and 950–980 cm^{-1}, respectively), and XANES simulations closely matching experimental data.[13,14] Collectively, these results establish W_3O_9 as the most representative WO_x structure on Pt nanoparticles under sub-monolayer conditions. It is to be noted that while the formation of W_1O_x or W_2O_x species on Pt is highly improbable, the presence of higher oligomeric structures (W_4O_x or beyond) cannot be categorically ruled out. W_3O_x on Pt is dynamic and expands catalytic chemistry possibilities.

Subsequent studies employing *in situ* Raman, UV-vis, Fourier transform infrared (FTIR) spectroscopy, DFT calculation, *tert*-butanol dehydration as a probe reaction, control systems of WO_x/SiO_2 and physical mixtures of Pt/SiO_2 and WO_x/SiO_2, revealed the existence and dynamics of distinct WO_x species.[13] Isolated WO_x on SiO_2 at low loadings are resilient to environmental changes, whereas the W_3O_x species on Pt nanoparticles are dynamic. Under annealed conditions, the W_3O_9 species are the most stable, reducing to W_3O_7 in an H_2/Ar environment at 673 K. However, one should note that the W_3O_7 sites are only partially reduced and remain active for dehydration. At lower temperatures, co-feeding H_2 transiently generates W–OH species (BAS) *via* protonation of terminal W=O bonds, forming W_3O_7H configurations and leading to an enhanced dehydration rate. These *in situ* BASs are more stable and active than the BASs associated with monomeric WO_x on SiO_2. Moreover, co-fed H_2O can also generate BASs by dissociating on terminal W sites (bridged W sites are energetically not favorable) of W_3O_x species. However, direct experimental evidence linking the unique performance of W_3O_x motifs on Pt over isolated WO_x sites on the support is still lacking.

BASs are critical for selective hydrogenolysis of polyols, such as glycerol and tetrahydrofurfuryl alcohol, to α,ω-diols.[6,21–24] These sites selectively cleave secondary C–O bonds by stabilizing cationic intermediates. A recent DFT study[25] demonstrated that the acid strength is vital in glycerol's C–O bond cleavage. Weak BASs possess high cleavage barriers for primary and secondary bonds. As the acid strength increases, the barrier difference decreases, and so does the selectivity to 1,3-propanediol (1,3-PDO). Strong BASs exhibit significant barrier differences, enabling selective cleavage of secondary bonds and enhanced 1,3-PDO formation.

Our earlier investigations[13,14] into inverse $WO_x/Pt/C$ (or SiO_2) catalysts showed that H_2 and H_2O pretreatments induce dynamic changes in WO_x BASs and redox sites depending on the pretreatment and timescales. At mild temperatures and high H_2 pressures, the BAS density increases over short timescales, but prolonged exposure dramatically increases the number of redox centers at the expense of BASs. Redox centers promote the undesired activation of primary hydroxyl groups in polyols and aromatic compounds.[5,17,26,27] H_2 modulation in WO_x/Pt catalysts can be used to alter the number of sites. It drives two competing effects: (*i*) selective generation of strong BASs over short timescales and (*ii*) undesired over-reduction of WO_x over longer timescales.

Despite the importance of these phenomena, experimental kinetics of these competing processes are sparse. The present work employs advanced transient spectroscopy and spectro-kinetic techniques under modulation to address this. Specifically, *in situ* UV-visible spectroscopy serves as a primary tool to investigate the active sites and the kinetics of reversible BAS and redox center formation on WO_x. Complementary techniques, including *in situ* Raman and IR spectroscopy, CO probe studies, and *tert*-butanol dehydration, further elucidate the impact of co-feeding of H_2O and H_2 partial pressure on catalytic activity, stability, and deactivation.

Experimental

Catalyst synthesis

The SiO_2 support was procured from Cabot Cab-O-Sil® (EH-5 grade, specific surface area ~332 m^2 g^{-1}).[28] For easy handling, the support was first hydrolysed with excess water, followed by overnight room temperature dying and calcination at 773 K for 4 h in static air. The obtained flakes were then crushed and sieved to obtain particle sizes of 100–150 μm. The pore volume of the support was measured to be 0.8 cc g^{-1} of SiO_2.

The incipient wetness impregnation method was followed to deposit Pt and WO_x onto the SiO_2 support. Specifically, the required amount of aqueous solution of chloroplatinic acid (Sigma Aldrich) was prepared and added dropwise to the SiO_2 support with vigorous mixing in a vortex mixer. The impregnated sample was then dried overnight at room temperature, followed by further drying at 393 K for 4 h in He flow and finally reduced at 873 K in 10% H_2/He flow for 2 h. For WO_x deposition, a required amount of aqueous solution of ammonium metatungstate (Sigma Aldrich) was prepared and added to the Pt/SiO_2 catalysts. The impregnated sample was then dried overnight at room temperature, followed by drying at 393 K for 2 h and calcination at 773 K for 4 h in static air. The samples are identified as $0.1Pt/SiO_2$, $1Pt/SiO_2$, $4 W-0.1Pt/SiO_2$ and $4 W-1Pt/SiO_2$. The numerical value in each catalyst represents the loading in the metal mass basis.

STEM (scanning tunnelling electron microscopy)

STEM imaging was done using a JEOL NEOARM microscope equipped with a spherical aberration corrector and two Energy-Dispersive X-Ray Spectroscopy (EDS) detectors operating at 200 kV. For this, the samples were dispersed using pure acetone solution onto lacey carbon-coated copper grids provided by Electron Microscopy Sciences. The diameter of over 100 particles was measured using the ImageJ software. The surface-weighted mean particle size was then calculated using the formula $\sum n_i d_i^3 / \sum n_i d_i^2$ (d_i, particle size; n_i, number of particles with size d_i).

HR-TEM (high resolution transmission electron microscopy) and HAADF-STEM-EDS (high angle annular dark field- STEM-EDS)

The distribution of Pt and W particles was further probed using a TITAN 80–300 aberration corrected TEM equipped with an EDS detector operating at 300 kV. For this, the samples were dispersed in pure ethanol and added onto lacey carbon-coated copper grids, provided by Electron Microscopy Sciences.

In situ Raman spectroscopy

Raman spectra were collected using a Horiba Jobin Yvon LabRAM high-resolution Raman apparatus equipped with 325, 532, and 633 nm laser excitations and a Syncerity OE detector. The 532 nm wavelength excitation was used to minimize sample damage by laser heating. Sample conditioning was carried out in a home built low void volume *in situ* cell.[29] The cell temperature was precisely controlled by an Omega temperature controller and cooling water flow. The gas flow was adjusted by mass flow controllers (MFCs). Before all experiments, the Raman laser was calibrated using a silicon standard. In a typical experiment, ~15–20 mg of catalyst in powder form was placed inside the sample cup of the *in situ* cell. A total of 150 s, 30 s per scan and 5 scans, were used for spectra acquisition.

In situ catalyst pre-treatment was undertaken before the *in situ* Raman measurements, as described below. Sample annealing was done at 673 K for 1 h in pure Ar flow (50 sccm). Sample reduction was undertaken in 10% H_2/Ar flow (50 sccm) at 673 K for 1 h, followed by purging with pure Ar at 673 K for another 30 minutes. After the pre-treatments, the sample temperature was decreased to 423 K for spectra collection in either pure Ar or 10% H_2/Ar flow (50 sccm). For catalyst reduction, the sample was additionally exposed to 10% H_2/Ar (50 sccm) gas flow for 2 h at 423 K.

CO-DRIFTS (diffuse reflectance infrared Fourier transform spectroscopy)

The CO-DRIFTS experiments were conducted in a Thermo Fisher Nicolet™ iS50 FTIR spectrometer. Sample conditioning was carried out in the Harrick environmental cell HVC-MRA-5. The cell temperature was precisely controlled by an ATK-024-3 Harrick temperature controller and cooling water flow. The gas flow was adjusted by mass flow controllers (MFCs). In a typical experiment, ~15–20 mg of catalyst in powder form was placed inside the sample cup of the *in situ* cell. 64 scans with a resolution of 4 cm^{-1} were used for spectra collection.

The sample pre-treatment was carried out as explained before. After the catalyst reduction and flushing at 673 K, the sample was cooled down to 308 K. 10% CO/Ar (10 sccm) was introduced for 15 minutes, followed by flushing with pure Ar for 30 minutes before spectra collection.

In situ UV-vis spectroscopy

UV–vis spectra were obtained using an Avantes ULS2048CL-EVO UV–vis spectrometer equipped with an AvaLight-XE light source and an adjustable UV/VIS/NIR high-temperature probe. The sample conditioning was carried out in a home built low void volume *in situ* cell. The cell temperature was precisely controlled by an Omega temperature controller and cooling water flow. The sample pre-treatment was done as mentioned for *in situ* Raman spectroscopy studies. For spectra collection after different pre-treatments, a total of 60 s, 0.1 s per scan and averaging over 600 scans, were used for spectral acquisition. $BaSO_4$ was used as the white reference material whose absorbance was subtracted from the sample absorbance spectra.

Transient spectroscopy study

Transient spectroscopy studies were conducted with *in situ* UV-vis spectroscopy. In all cases, the samples were pre-reduced and flushed at 673 K as mentioned in the *in situ* Raman spectroscopy experimental procedure. The sample was then cooled to 423 K, where all other investigations were undertaken. For all kinetic measurements, a total of 1 s, 0.1 s per scan and averaging over 10 scans, were used for spectral acquisition. The home built *in situ* cell has a void volume of <1 cc, suggesting the gases have an average residence time of <1.2 s at total flow of 50 sccm.[29]

The modulation excitation UV-visible spectroscopy (ME-UV-vis) experiment was conducted by alternately exposing the catalyst bed to 10% H_2/Ar for 900 s and pure Ar for 900 s in a cyclic manner (1800 s per cycle). The fast gas switching was ensured by implementing a Vici low dead volume valve with automatic operation functionality. A home-built software was used to analyse the MES data. A total of 5 cycles of gas switching was conducted, out of which the last 3 cycles were averaged for data interpretation. The fundamental frequency (f_1) was used to understand the dynamic response of participating sites to feed perturbation.

BAS kinetics were determined by step-jump experiments. In particular, in a 900 s cycle, 10% H_2/Ar was introduced into the catalyst bed for the first 120 s, and the system was then exposed to pure Ar for the remaining 780 s. An average of 4 cycles were used to process the data. The change in the
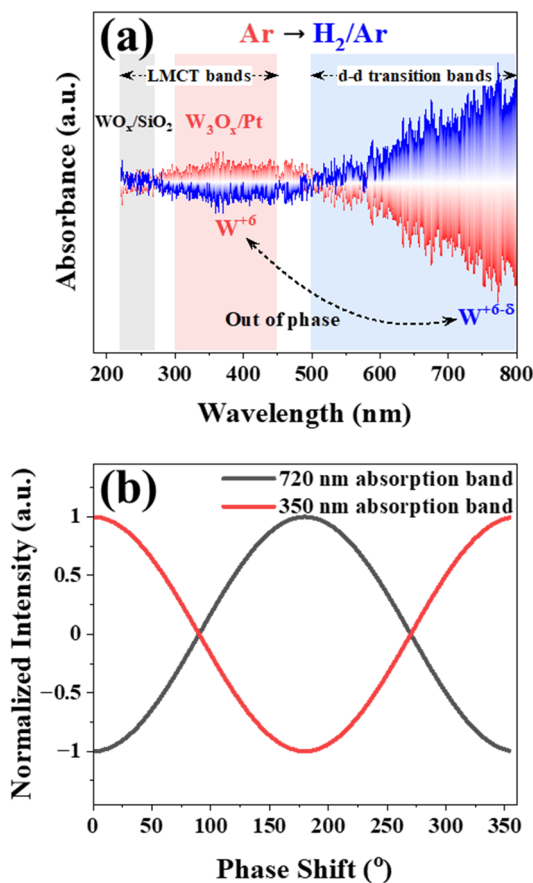
Fig. 1 (a) ME UV-vis phase-resolved spectra of the 4 W–1Pt/SiO$_2$ catalyst. Cycle length is 1800 s, with the 1st half cycle of 10% H$_2$/Ar and 2nd half cycle in pure Ar. Only the fundamental frequency (f_1) was used to generate the plot. (b) Phase response of normalized 720 nm and 350 nm band intensities.

absorbance intensity of the 720 nm band (assigned to reduced WO$_x$ species) was used to measure the kinetics of the processes. A first-order approximation was taken to model the WO$_x$ hydroxylation to determine the rate constant ($k_{d(BAS)}$) for BAS decomposition as shown in eqn (1). For

determining the rate ($r_{d(BAS)}$) of BAS decomposition, a liner fit of the absorbance was used for the 60 s period (121–180 s) after the gas switching from 10% H$_2$/Ar to Ar (refer to Fig. 4 for demonstration.)

$$I(C_{BAS}) = I(C'_{BAS}) + I(C_{BAS_0})\exp(-k_{d(BAS)} \cdot t); \qquad (1)$$

where, $I(C_{BAS})$ represents the UV-vis intensity of the 720 nm band related to the concentration of BASs at time t; $I(C'_{BAS})$ is a constant related to the 720 nm band intensity in the absence of any BAS formation; $I(C_{BAS_0})$ represents the UV-vis intensity of the 720 nm band related to the concentration of BASs at time 0, initial time; $k_{d(BAS)}$ is the rate constant for BAS decomposition; t is time.

To obtain the catalyst reduction kinetics, the sample was exposed to Ar, 10% H$_2$/Ar, 2% H$_2$/Ar and (10% H$_2$ + 3% H$_2$O)/Ar for different durations. A representative schematic is shown in Fig. S8. After each treatment duration, the rate of BAS decomposition ($r_{d(BAS)}$) was then determined. Since the rate of a chemical reaction is directly proportional to the concentration of the active species, any variation in their concentration is reflected in the overall reaction rate. To quantify this, the relative change in concentration was evaluated by taking the ratio of reaction rates after catalyst conditioning in the above-mentioned gas environments to the rate prior to any conditioning. Specifically, the concentration of available BASs was inferred from the absolute reaction rates measured at defined time intervals. By comparing the rate at time $t = \Delta t$ to the initial rate at $t = 0$ (where Δt refers to the duration of catalyst treatment in different gas environments), we estimated the relative decline in the population of BAS-forming sites. This approach enabled us to track the progressive reduction of W$_3$O$_7$H species as a function of time and gas environment. Finally, a first-order approximation was employed to model the reduction kinetics of WO$_x$ species, allowing the determination of the apparent rate constant (k_{red}).
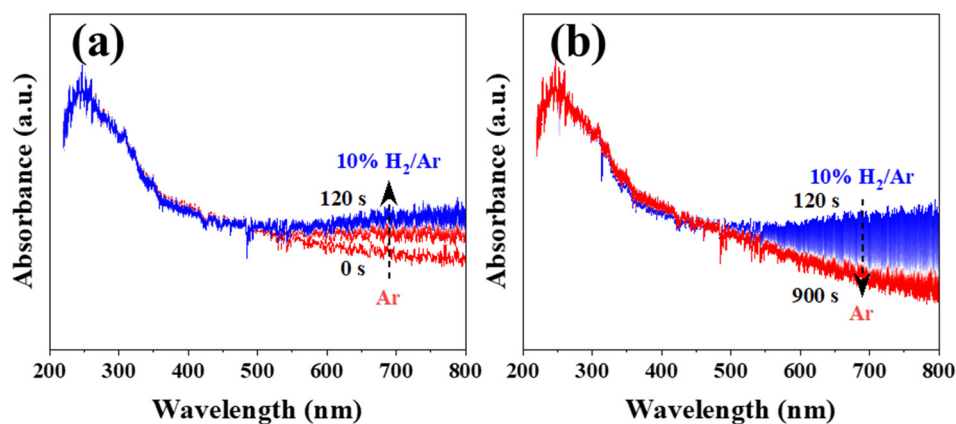

Fig. 2 Time-resolved UV-vis spectra of the 4 W–1Pt/SiO$_2$ catalyst. The H$_2$ on–off cycle duration is 900 s, where (a) 10% H$_2$/Ar was introduced for the first 120 s and (b) pure Ar for the remaining 780 s.
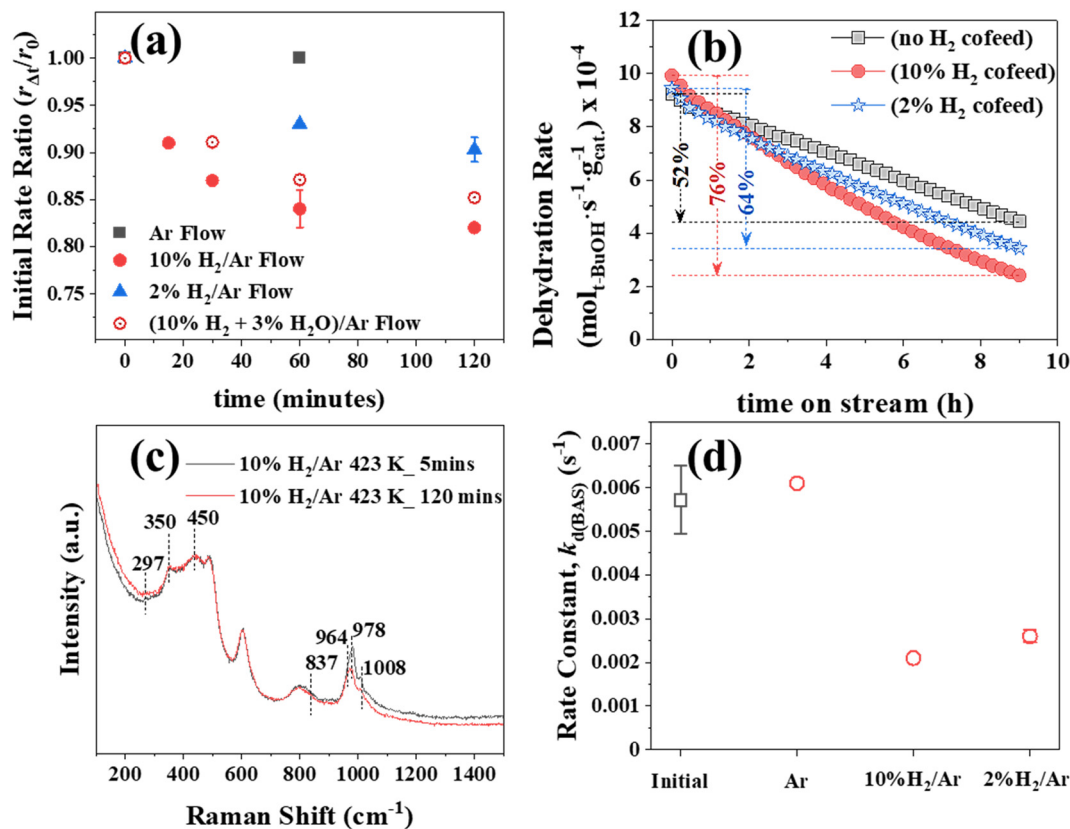
Fig. 3 Slow reduction of the 4 W–1Pt/SiO$_2$ catalyst. (a) BAS decomposition initial rate ratio (of Δt minutes' treatment to no treatment in Ar, 2% H$_2$/Ar, 10% H$_2$/Ar and (10% H$_2$ + 3% H$_2$O)/Ar) calculated from UV-vis spectroscopy (see Fig. S8 and the associated discussion). (b) Time on stream t-butanol activity without H$_2$ co-feed, and with 2% and 10% H$_2$ co-feed. The values in the plot represent the percentage decrease in activity after 9 h as compared to the initial activity. (c) *In situ* Raman spectra in 10% H$_2$/Ar environment (after 5 and 120 min of treatment). (d) BAS decomposition rate constant ($k_{d(BAS)}$) after 120 minutes' treatment in Ar, 2% H$_2$/Ar and 10% H$_2$/Ar. All catalysts were pre-reduced at 673 K in 10% H$_2$/Ar for 60 min. All experiments were conducted at 423 K.

CO-pulse chemisorption

The CO pulse chemisorption experiments were carried out in a Micromeritics Autochem-II 2920 analyzer equipped with a TCD detector. In a typical experiment, ~50 mg of powder catalyst was loaded into a quartz U-tube. The catalyst reduction and flushing were conducted at 673 K as described before. The temperature was then decreased to 308 K, and CO adsorption was carried out by pulse injection of 10% CO/He until the sample was saturated. For investigating catalyst reduction, the sample was additionally exposed to 10% H$_2$/Ar (50 sccm) gas flow for 2 h at 423 K before cooling down to 308 K.

tert-Butanol dehydration

The *tert*-butanol dehydration was carried out in a fixed bed reactor. 2 mg of the catalyst, diluted by 48 mg of quartz were loaded and put in place by the help of quartz wool.[13] Before the dehydration reaction, the sample was reduced and flushed at 673 K as described before. The temperature was then lowered to 423 K. 4 mol% *tert*-butanol was admitted into the reactor through a customized gas saturator. The total gas flow rate was balanced in N$_2$ at 100 sccm. *tert*-Butanol

conversion was calculated using eqn (2), as carbon balance of >95% was observed.

$$\textit{tert-butanol conversion}(\%)$$
$$= \frac{(\textit{tert-butanol in(mol)}) - (\textit{tert-butanol out(mol)})}{(\textit{tert-butanol in(mol)})} \times 100\% \tag{2}$$

Results and discussion

We synthesized a library of materials (see Experimental) denoted as xW–yPt/SiO$_2$, where x and y reflect the weight percent of WO$_x$ and Pt on the SiO$_2$ support, respectively. Detailed characterization of inverse WO$_x$/Pt on SiO$_2$ catalysts is presented in SI section 1 (see Fig. S1–S4 and the associated discussion). In brief, 1Pt/SiO$_2$ and 0.1Pt/SiO$_2$ catalysts have Pt particles of comparable sizes, ~1.7–2 nm. Adding WO$_x$ does not significantly alter the Pt particle size, although a slight increase is observed for the 0.1Pt/SiO$_2$ catalyst. For the 4 W–1Pt/SiO$_2$ catalyst, reduction at 673 K results in approximately 2/3rd of the exposed Pt surface being decorated by WO$_x$ species, confirming the inverse WO$_x$/Pt configuration formation. The following uses the 4 W–1Pt/SiO$_2$ as a representative catalyst.
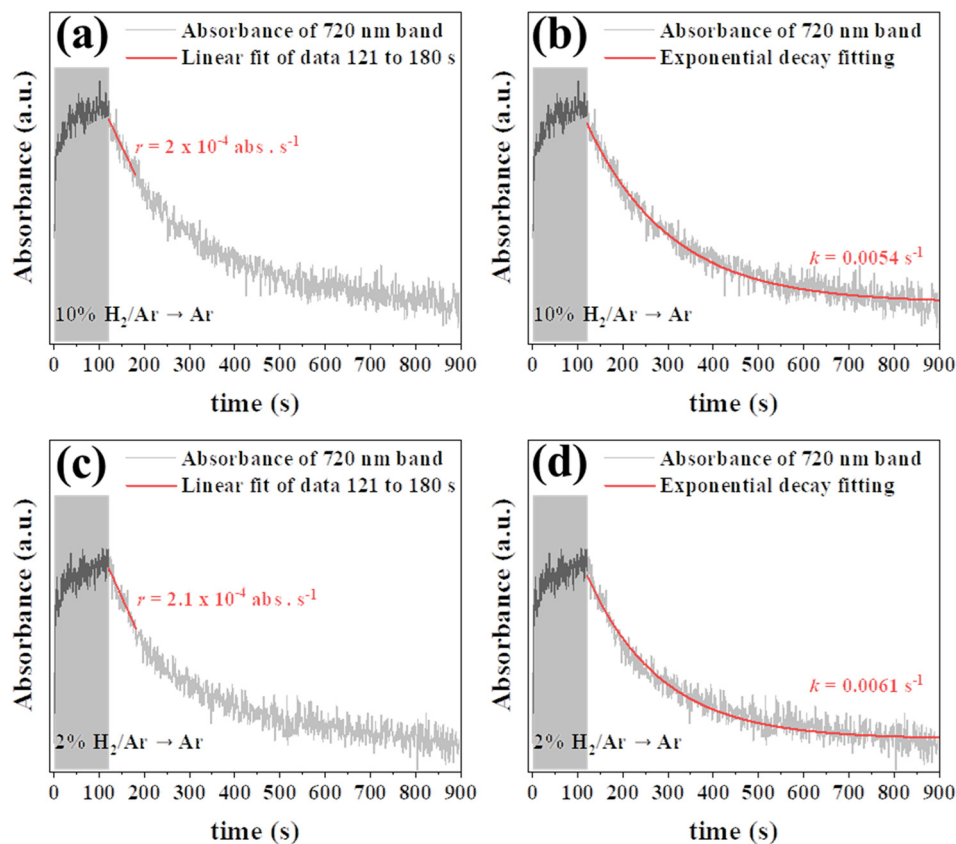
Fig. 4 Effect of H_2 partial pressure on the BAS formation and decomposition on the 4 W-1Pt/SiO$_2$ catalyst. (a) The BAS decomposition rate $r_{d(BAS)}$, and (b) BAS decomposition rate constant ($k_{d(BAS)}$) after removal of 10% H_2/Ar. (c) The BAS decomposition rate $r_{d(BAS)}$, and (d) BAS decomposition rate constant ($k_{d(BAS)}$) after removal of 2% H_2/Ar. The cycle duration is 900 s, where H_2/Ar was introduced for the first 120 s and pure Ar for the remaining 780 s. The $r_{d(BAS)}$ was calculated by taking a linear approximation of between 121 and 180 s (60 s duration after H_2 removal) and $k_{d(BAS)}$ was calculated by exponential decay fitting of absorbance data from 121 to 900 s. All catalysts were pre-reduced at 673 K in 10% H_2/Ar for 60 minutes. All experiments were conducted at 423 K.

Identifying the active site for *in situ* BAS formation

In situ Raman and UV-visible spectroscopy reveal that the 4 W-1Pt/SiO$_2$ catalyst comprises two distinct WO$_x$ species: (*i*) isolated WO$_x$ units on the SiO$_2$ support and (*ii*) W$_3$O$_x$ units associated with Pt nanoparticles (see SI section 2, Fig. S5 and the accompanying discussion). These results are consistent with prior reports.[13] To unequivocally identify the active WO$_x$ site responsible for forming *in situ* the BASs (see SI section 3 for the detailed discussion), we conducted modulation excitation UV-visible (ME UV-vis) spectroscopy experiments (see Fig. 1). In these experiments, the catalyst bed was alternately exposed to 10% H_2/Ar for 900 s and pure Ar for 900 s in a cyclic manner (1800 s cycle duration). The dynamic response for the WO$_x$ structure to feed perturbation was analyzed using the fundamental frequency, providing critical insights into the WO$_x$ species under reaction conditions.[30]

Phase-resolved spectra for the 4 W-1Pt/SiO$_2$ catalyst (Fig. 1a) reveal dynamic changes in the ligand-to-metal charge transfer (LMCT) bands and the *d–d* transition region, absent from the 1Pt/SiO$_2$ and 4 W/SiO$_2$ catalysts (see SI section 4, Fig. S6 and the associated discussion). Among the

LMCT bands, only those associated with W$_3$O$_x$ species on Pt (300–450 nm)[13] show variations, whereas the LMCT bands of isolated WO$_x$ sites on SiO$_2$ (220–270 nm)[20,31] remain unchanged during H_2 switching. This is the first direct experimental evidence of *in situ* BAS formation on selective W$_3$O$_x$ units on Pt and rules out the participation of isolated WO$_x$ sites on SiO$_2$.

Interestingly, the LMCT band at ~350 nm and the reduced WO$_x$ absorption band at ~720 nm[20] exhibit a 180° phase difference (Fig. 1b). This indicates that the hydroxylation of W$_3$O$_x$ units on Pt is reversible, where BASs form by gas-phase H_2 temporarily, and the reduced W centers regain the original oxidation state upon the removal of H_2 from the gas phase, closing the redox cycle.[13]

Structural evolution of the 4 W-1Pt/SiO$_2$ catalyst

The dynamic evolution of the 4 W-1Pt/SiO$_2$ catalyst is detailed in SI section 2 (see Fig. S5 and the associated discussion). As shown in the previous section, W$_3$O$_x$ units on Pt exhibit structural dynamics under controlled conditions. Catalyst treatment in H_2 at 673 K reduces fully oxidized W$_3$O$_9$ units to

W_3O_7 units. Subsequently, introducing H_2 at 423 K to the pre-reduced catalyst forms BASs as a W_3O_7H configuration.[13]

The correlation between *in situ* Raman and UV-visible experiments indicates that the dynamics of W_3O_x sites can be accurately captured using *in situ* UV-visible spectroscopy. In particular, the reversible formation of BASs during periodic H_2 on–off cycling in the catalyst bed can be monitored *via* the intensity of the 720 nm band in the UV-visible spectra (see SI section 2). Given the rapid data acquisition capability of UV-visible spectroscopy (~0.1 s per spectrum) compared to the slower Raman spectroscopy (~several minutes per spectrum), *in situ* UV-visible spectroscopy was employed as the primary tool to investigate the kinetics of reversible BAS formation and decomposition.

Kinetics of the formation and decomposition of BASs in the 4 W-1Pt/SiO₂ catalyst

The catalyst was exposed to 10% H_2/Ar for 120 s, followed by pure Ar for 780 s, in a 900 s cycle. The 720 nm absorption band was monitored to track BAS kinetics, with time-resolved UV-visible spectra presented in Fig. 2, and the intensity evolution of the 720 nm band shown in Fig. S7 (see SI section 5).

Fig. S7 reveals that BASs form within seconds of H_2 introduction, while decomposition upon H_2 removal occurs over 780 s. Assuming first-order kinetics of the BAS decomposition by H atom removal from the –OH group in W_3O_7H, the decomposition rate constant ($k_{d(BAS)}$) for the 4 W-1Pt/SiO₂ was estimated as $5.7 \pm 0.1 \times 10^{-3}$ s^{-1} (see Table 1) and for 4 W-0.1Pt/SiO₂, ($k_{d(BAS)}$) is $4 \pm 0.1 \times 10^{-3}$ s^{-1}. Despite differences in WO_x distribution (on the SiO₂ support and Pt nanoparticles) between catalysts, the similar $k_{d(BAS)}$ values confirm that only WO_x sites on Pt in the inverse WO_x/Pt configuration undergo dynamic changes, while isolated WO_x sites on SiO₂ do not. The rapid BAS formation (Fig. S7) suggests that the corresponding rate constant ($k_{f(BAS)}$) is at least two orders of magnitude higher (see Table 1) under the investigated conditions, further highlighting the unique reactivity of WO_x sites on Pt.

Kinetics and origin of slow reduction of the 4 W-1Pt/SiO₂ catalyst

The rate constant for BAS decomposition, $k_{d(BAS)}$, reveals information about the nature of the active sites, while the initial decomposition rate is proportional to the concentration of BASs. Variations in the initial BAS decomposition rates after prolonged exposure to H_2/Ar *vs.* inert Ar environments shed light on the gradual irreversible reduction of the catalyst at the expense of BASs (see SI section 6). This behavior is captured with the ratio of initial BAS decomposition rates, $r_{\Delta t}/r_0$, where $r_{\Delta t}$ is the rate after treatment duration of Δt, and r_0 is the rate before any treatments (see Fig. 3a).

Exposure to Ar results in no change in $r_{\Delta t}/r_0$, whereas treatment with 10% H_2/Ar rapidly decreases $r_{\Delta t}/r_0$ within the first 30 min, followed by a slower decline. Assuming a first-order process in the catalyst reduction, driven by the removal of the –OH group from W_3O_7H by an H atom to generate W_3O_6, we determined the reduction rate constant for site reduction (k_{red}, see Table 1). Notably, the k_{red} of the 4 W-1Pt/SiO₂ catalyst is an order of magnitude lower than the $k_{d(BAS)}$ and almost 3 orders of magnitude lower than the $k_{f(BAS)}$.

The catalyst reduction is further evident from the decrease in *tert*-butanol dehydration rates; see Fig. 3b. To understand the origin of catalyst reduction, we conducted CO-pulse chemisorption and *in situ* Raman studies. The WO_x coverage on Pt does not change under prolonged H_2 pre-treatment conditions (see Fig. S3), suggesting the decrease in activity (and BAS concentration) is unrelated to WO_x migration from the Pt nanoparticles to the SiO₂ support. *In situ* Raman studies reveals that the reduction of WO_x species occurs specifically on Pt nanoparticles (see Fig. 3c). The terminal W=O (978 and 297 cm^{-1} band) is more susceptible to reduction than the bridging W=O. In contrast, W–O–W and Pt–O–W (450 and 837 cm^{-1})[13] remain unaffected. Since BAS formation is associated with terminal W=O bonds,[13] their reduction significantly alters the nature and concentration of BASs. This is supported by the drastic decrease in $k_{d(BAS)}$ (see Fig. 3d) after H_2/Ar treatment. This is the first experimental evidence revealing the origin of BAS reduction in WO_x/Pt inverse catalysts. Furthermore, the above *in situ* Raman characterization demonstrates that the terminal W=O bonds in WO_x/Pt inverse catalysts are where the BASs form. This finding is further supported by our previous DFT calculations,[14] which showed that H_2 dissociation on terminal W=O bonds is energetically favored by 1.10 eV compared to bridging W–O–W bonds, facilitating BAS formation.

Effect of co-feed H₂O on the reduction kinetics of the 4 W-1Pt/SiO₂ catalyst

Our previous DFT calculations and experimental studies have demonstrated that co-feeding H_2O enhances BAS density.[14]

Table 1 Kinetics of formation ($k_{f(BAS)}$), decomposition ($k_{d(BAS)}$) of BASs and slow reduction (k_{red}) of WO_x species with periodic H_2 on–off and long-term H_2 and $H_2 + H_2O$ flow, respectively. All catalysts were pre-reduced at 673 K in 10% H_2/Ar for 60 minutes. The rate constants were determined at 423 K

k (s^{-1})	4 W-1Pt/SiO₂			4 W-0.1Pt/SiO₂
	10% H_2/Ar	2% H_2/Ar	(10% H_2 + 3% H_2O)/Ar	10% H_2/Ar
$k_{f(BAS)}$	$>10^0$			
$k_{d(BAS)}$	$5.7 \pm 0.1 \times 10^{-3}$	$6.5 \pm 0.1 \times 10^{-3}$		$4 \pm 0.1 \times 10^{-3}$
k_{red}	$\sim 7.2 \times 10^{-4}$	$\sim 2.6 \times 10^{-4}$	$\sim 4.9 \times 10^{-4}$	

To investigate the competitive effects of H_2 and H_2O on BAS formation and reduction under prolonged exposure, the catalyst was conditioned in a 10% H_2 + 3% H_2O environment for varying durations (Fig. 3a). Notably, in the presence of H_2O, the site reduction rate constant (k_{red}, see Table 1) was suppressed by 50% compared to the dry 10% H_2/Ar conditions.

Effect of H_2 partial pressure

While H_2 facilitates rapid, reversible BAS generation on a short timescale, prolonged exposure leads to undesirable catalyst irreversible reduction. To address this, we investigated the impact of H_2 partial pressure on BAS formation and catalyst reduction to identify optimized process conditions.

On short timescales, the H_2 partial pressure (2% *vs.* 10%) has a negligible effect on the initial rate and rate constant for BAS decomposition, suggesting that the BAS concentration weakly depends on the H_2 partial pressure (see Fig. 4 and Table 1). This is also reflected in the marginal change in the initial dehydration activity (see Fig. 3b). However, over extended periods, the state of the catalyst is significantly affected by the H_2 partial pressure (see Fig. 3a). The rate constant of reduction (k_{red}) (see Table 1) shows that the catalyst reduction is ~3× slower in 2% H_2/Ar stream than in 10% H_2/Ar stream. This trend is observed in the time on stream dehydration activity data (see Fig. 3b), where, despite slightly lower initial dehydration activity, the catalyst under 2% H_2 co-feed conditions outperforms that under 10% H_2 co-feed conditions over an extended reaction time.

Conclusions

The dynamic formation, decomposition, and reduction of Brønsted acid sites (BASs) in the inverse WO_x/Pt catalyst were investigated using advanced spectro-kinetic techniques. *In situ* Raman and UV-visible spectroscopy identified two types of WO_x sites: (*i*) isolated WO_x species on the SiO_2 support, and (*ii*) polymeric W_3O_x species on Pt nanoparticles. Modulation Excitation UV-visible spectroscopy (ME UV-vis), for the first time, revealed that WO_x units on Pt nanoparticles undergo dynamic changes during gas environment modulation while isolated WO_x sites on SiO_2 remain unaffected.

UV-visible spectro-kinetics experiments unveiled the underlying kinetics of these processes, demonstrating that the rate constant for the reversible BAS formation is at least two orders of magnitude higher than that of its decomposition, which is itself an order of magnitude higher than that of irreversible site reduction. *In situ* Raman spectroscopy further revealed that catalyst reduction primarily occurs by removing terminal W=O bonds, catalytic active sites for BAS formation, of W_3O_x after prolonged exposure to an H_2 environment. Interestingly, co-feeding of H_2O suppresses the reduction of the terminal W=O bond by 50%, which is attributed to the role of H_2O towards partial

oxidation of the reduced sites.[10,14] In addition, the H_2 partial pressure plays a crucial role in catalyst dynamics. While BAS reversible formation kinetics and steady-state dehydration activity do not show significant dependence on H_2 partial pressure, lower H_2 partial pressures significantly mitigate catalyst deactivation. Multiscale models, built using density functional theory and microkinetics, could follow the oxidation and reduction of individual sites and expose the catalyst dynamics when H_2 and H_2O co-exist, *e.g.*, as a reactant and a product. They both can protonate WO_x, whereas H_2 (H_2O) can also reduce (oxidize) WO_x at longer times. Alternatively, the development of rate expressions from experiments with feeding H_2 or H_2O only could also help understand the catalyst state when H_2 and H_2O co-exist in the reactor.

These findings provide valuable insights into optimizing process conditions for enhanced stability and efficiency of WO_x/Pt inverse catalysts, offering a pathway to more sustainable catalytic processes.

Conflicts of interest

The authors declare no competing interest.

Data availability

All data used in the publication can be obtained from the corresponding author upon reasonable request. Supplementary information (SI) is available. See DOI: https://doi.org/10.1039/d5cy00917k

Acknowledgements

References

1   J. C. Védrine, *Heterogeneous Catalysis on Metal Oxides Catalysts [Online]*, 2017.

2   K. Tomishige, Y. Nakagawa and M. Tamura, Selective hydrogenolysis and hydrogenation using metal catalysts directly modified with metal oxide species, *Green Chem.*, 2017, **19**(13), 2876–2924.

3   M. Chia, Y. J. Pagán-Torres, D. Hibbitts, Q. Tan, H. N. Pham, A. K. Datye, M. Neurock, R. J. Davis and J. A. Dumesic, Selective Hydrogenolysis of Polyols and Cyclic Ethers over Bifunctional Surface Sites on Rhodium–Rhenium Catalysts, *J. Am. Chem. Soc.*, 2011, **133**(32), 12675–12689.

4 O. M. Daniel, A. DeLaRiva, E. L. Kunkes, A. K. Datye, J. A. Dumesic and R. J. Davis, X-ray Absorption Spectroscopy of Bimetallic Pt–Re Catalysts for Hydrogenolysis of Glycerol to Propanediols, *ChemCatChem*, 2010, **2**(9), 1107–1114.

5 C. Wang, A. V. Mironenko, A. Raizada, T. Chen, X. Mao, A. Padmanabhan, D. G. Vlachos, R. J. Gorte and J. M. Vohs, Mechanistic Study of the Direct Hydrodeoxygenation of m-Cresol over WOx-Decorated Pt/C Catalysts, *ACS Catal.*, 2018, **8**(9), 7749–7759.

6 C. Wang, J. D. Lee, Y. Ji, T. M. Onn, J. Luo, C. B. Murray and R. J. Gorte, A Study of Tetrahydrofurfuryl Alcohol to 1,5-pentanediol Over Pt–WOx/C, *Catal. Lett.*, 2018, **148**(4), 1047–1054.

7 F. Yang, N. J. Libretto, M. R. Komarneni, W. Zhou, J. T. Miller, X. Zhu and D. E. Resasco, Enhancement of m-Cresol Hydrodeoxygenation Selectivity on Ni Catalysts by Surface Decoration of MoOx Species, *ACS Catal.*, 2019, **9**(9), 7791–7800.

8 W. Zhou, Y. Li, X. Wang, D. Yao, Y. Wang, S. Huang, W. Li, Y. Zhao, S. Wang and X. Ma, Insight into the nature of Brönsted acidity of Pt-(WOx)n-H model catalysts in glycerol hydrogenolysis, *J. Catal.*, 2020, **388**, 154–163.

9 J. Zhou, A. Worrad, Y. Wang, K. Yu, S. Deshpande, J. A. Boscoboinik, S. Caratzoulas, W. Zheng and D. G. Vlachos, The role of the metal core in the performance of WOx inverse catalysts, *Chem Catal.*, 2023, **3**(10), 100756.

10 J. Zhou, J. Fu, P. Yang, K. Yu, S. Caratzoulas, W. Zheng and D. G. Vlachos, Controlling oxide promoter coverage and microstructure on metals of inverse catalysts: Application to liquid phase tetrahydrofurfuryl alcohol conversion to 1,5-pentanediol, *Appl. Catal. B: Environ.*, 2024, **346**, 123724.

11 K. M. Nicholas, *Selective catalysis for renewable feedstocks and chemicals*, Springer, 2014, vol. 353.

12 J. He, K. Huang, K. J. Barnett, S. H. Krishna, D. M. Alonso, Z. J. Brentzel, S. P. Burt, T. Walker, W. F. Banholzer, C. T. Maravelias, I. Hermans, J. A. Dumesic and G. W. Huber, New catalytic strategies for α,ω-diols production from lignocellulosic biomass, *Faraday Discuss.*, 2017, **202**, 247–267.

13 Y. Wu, S. Sourav, A. Worrad, J. Zhou, S. Caratzoulas, G. Tsilomelekis, W. Zheng and D. G. Vlachos, Dynamic Formation of Brönsted Acid Sites over Supported WOx/Pt on SiO2 Inverse Catalysts–Spectroscopy, Probe Chemistry, and Calculations, *ACS Catal.*, 2023, **13**(11), 7371–7382.

14 J. Fu, S. Liu, W. Zheng, R. Huang, C. Wang, A. Lawal, K. Alexopoulos, S. Liu, Y. Wang, K. Yu, J. A. Boscoboinik, Y. Liu, X. Liu, A. I. Frenkel, O. A. Abdelrahman, R. J. Gorte, S. Caratzoulas and D. G. Vlachos, Modulating the dynamics of Brönsted acid sites on PtWOx inverse catalyst, *Nat. Catal.*, 2022, **5**(2), 144–153.

15 C. Wei, G. Zhang, L. Zhao, J. Gao and C. Xu, Effect of metal–acid balance and textual modifications on hydroisomerization catalysts for n-alkanes with different chain length: A mini-review, *Fuel*, 2022, **315**, 122809.

16 E. Eßer, D. Schröder, A. V. Nartova, A. M. Dmitrachkov and S. Kureti, Reduction of NOx by H2 on WOx-Promoted Pt/Al2O3/SiO2 Catalysts Under O2-Rich Conditions, *Catal. Lett.*, 2022, **152**(6), 1598–1610.

17 D. Zhang, Q. Zhang, Z. Zhou, Z. Li, K. Meng, T. Fang, Z. You, G. Zhang, B. Yin, J. Shen, C. Yang, W. Yan and X. Jin, Hydrogenolysis of Glycerol to 1,3-Propanediol: Are Spatial and Electronic Configuration of "Metal-Solid Acid" Interface Key for Active and Durable Catalysts?, *ChemCatChem*, 2022, **14**(2), e202101316.

18 T. Tan, W. Wang, K. Zhang, Z. Zhan, W. Deng, Q. Zhang and Y. Wang, Upcycling Plastic Wastes into Value-Added Products by Heterogeneous Catalysis, *ChemSusChem*, 2022, **n/a**(n/a), e202200522.

19 J. Marlowe, S. Deshpande, D. G. Vlachos, M. M. Abu-Omar and P. Christopher, Effect of Dynamic and Preferential Decoration of Pt Catalyst Surfaces by WOx on Hydrodeoxygenation Reactions, *J. Am. Chem. Soc.*, 2024, **146**(20), 13862–13874.

20 S. Lwin, Y. Li, A. I. Frenkel and I. E. Wachs, Nature of WOx Sites on SiO2 and Their Molecular Structure–Reactivity/Selectivity Relationships for Propylene Metathesis, *ACS Catal.*, 2016, **6**(5), 3061–3071.

21 S. García-Fernández, I. Gandarias, J. Requies, F. Soulimani, P. L. Arias and B. M. Weckhuysen, The role of tungsten oxide in the selective hydrogenolysis of glycerol to 1,3-propanediol over Pt/WOx/Al2O3, *Appl. Catal., B*, 2017, **204**, 260–272.

22 K. J. Stephens, A. M. Allgeier, A. L. Bell, T. R. Carlson, Y. Cheng, J. T. Douglas, L. A. Howe, C. A. Menning, S. A. Neuenswander, S. K. Sengupta, P. S. Thapa and J. C. Ritter, A Mechanistic Study of Polyol Hydrodeoxygenation over a Bifunctional Pt-WOx/TiO2 Catalyst, *ACS Catal.*, 2020, **10**(21), 12996–13007.

23 L. Liu, J. Cao, Y. Nakagawa, M. Betchaku, M. Tamura, M. Yabushita and K. Tomishige, Hydrodeoxygenation of C4–C6 sugar alcohols to diols or mono-alcohols with the retention of the carbon chain over a silica-supported tungsten oxide-modified platinum catalyst, *Green Chem.*, 2021, **23**(15), 5665–5679.

24 Z. Lin, S. Liu, S. R. Denny, W. N. Porter, S. Caratzoulas, J. A. Boscoboinik, D. G. Vlachos and J. G. Chen, Experimental and Theoretical Insights into the Active Sites on WOx/Pt(111) Surfaces for Dehydrogenation and Dehydration Reactions, *ACS Catal.*, 2021, **11**(13), 8023–8032.

25 A. Rajan and J. J. Varghese, Towards selective glycerol hydrodeoxygenation to 1,3-propanediol with effective Pt-WOx catalyst design: Insights from first principles, *J. Catal.*, 2023, **423**, 94–104.

26 K. Murugappan, E. M. Anderson, D. Teschner, T. E. Jones, K. Skorupska and Y. Román-Leshkov, Operando NAP-XPS unveils differences in MoO3 and Mo2C during hydrodeoxygenation, *Nat. Catal.*, 2018, **1**(12), 960–967.

27 S. Deo, W. Medlin, E. Nikolla and M. J. Janik, Reaction paths for hydrodeoxygenation of furfuryl alcohol at TiO2/Pd interfaces, *J. Catal.*, 2019, **377**, 28–40.

28 S. Sourav, Y. Wang, D. Kiani, J. Baltrusaitis, R. R. Fushimi and I. E. Wachs, New Mechanistic and Reaction Pathway Insights for Oxidative Coupling of Methane (OCM) over Supported Na2WO4/SiO2 catalysts, *Angew. Chem., Int. Ed.*, 2021, **60**(39), 21502–21511.

29 B. S. Patil, P. D. Srinivasan, E. Atchison, H. Zhu and J. J. Bravo-Suárez, Design, modelling, and application of a low void-volume in situ diffuse reflectance spectroscopic reaction cell for transient catalytic studies, *React. Chem. Eng.*, 2019, **4**(4), 667–678.

30 P. D. Srinivasan, B. S. Patil, H. Zhu and J. J. Bravo-Suárez, Application of modulation excitation-phase sensitive detection-DRIFTS for in situ/operando characterization of heterogeneous catalysts, *React. Chem. Eng.*, 2019, **4**(5), 862–883.

31 E. I. Ross-Medgaarden and I. E. Wachs, Structural Determination of Bulk and Surface Tungsten Oxides with UV−vis Diffuse Reflectance Spectroscopy and Raman Spectroscopy, *J. Phys. Chem. C*, 2007, **111**(41), 15089–15099.